ADVANCED FUNCTIONAL MATERIALS
www.afm-journal.de

Localized Laser-Based Photohydrothermal Synthesis of Functionalized Metal-Oxides

*Kyungmook Kwon, Jaeho Shim, Jeong Oen Lee, Kyunghan Choi, and Kyoungsik Yu**

We discuss the rapid in situ hydrothermal synthesis of metal oxide materials based on the photothermal superheating of light-absorbing metal layers for simple and facile on-demand placement of semiconductor materials with micrometer-scale lateral resolution. Localized heating from pulsed and focused laser illumination enables ultrafast growth of metal oxide materials with high spatiotemporal precision in aqueous precursor solution. Among many possible electronic and optoelectronic applications, the proposed method can be used for laser-based in situ real-time soldering of separated metal structures and electrodes with functionalized semiconductor materials. Resistive electrical interconnections of metal strip lines as well as sensitive UV detection using photohydrothermally grown metal oxide bumps are experimentally demonstrated.

1. Introduction

Metal-oxides have attracted much attention over the past few decades for their wide range of applications. Due to the strong ionic bonds between positive metallic and negative oxygen ions, semiconducting metal oxide materials provide interesting and unique characteristics, such as wide bandgaps,[1] good electrical and thermal conductivities,[2] and thermal/chemical stability.[3] The localized formation of metal-oxides between metal micro/nanostructures not only allows structural and mechanical joining at the submicrometer scale but also can provide additional electrical semiconducting functionalities. For example, when the metal oxide materials, such as zinc oxide, are inserted between metal electrodes, they can provide memristive,[4] gating,[5] or rectifying electrical connections.[6] They are also responsive to physical and environmental stimuli such as UV illumination,[7] pressure,[8] ambient chemicals,[9] and/or humidity,[10] and thus can serve as sensing elements in a chip-scale integrated sensor platform. The localized photohydrothermal metal-oxides synthesis technique demonstrated in this work can be readily used in a number of applications including resistive electrical interconnections between two metal strip lines as well as sensitive detection of UV illumination at the wavelength-scale dimensions.

To achieve the facile single-step direct synthesis of metal-oxides at a desired position with small feature sizes, we use a highly localized hydrothermal method with pulsed-light-induced heating (PLIH) on planar metal thin films and/or strip structures with pulsed and focused laser irradiation. PLIH provides an efficient way to manipulate the spatiotemporal temperature distribution near the laser beam spot in precursor solution, and thereby to thermally stimulate hydrothermal synthesis reactions[11,12] with precise spatial and temporal control. In the proposed method, the local temperature of precursor solution near the focused laser beam spot during the illumination can easily exceed the boiling point at normal ambient pressure through periodic thermal cycles from the pulsed illumination and superheating.[13] Superheating far above the typical boiling point enables a much faster metal-oxide growth rate[14] as compared to conventional large-area hydrothermal growth using a bulk heating method.[11,12] Repetitive heating and cooling from PLIH prevents explosive bubble generation even beyond the superheating condition[15] as schematically described in Figure S1, Supporting Information. A steep temperature gradient around the laser beam spot results in strong precursor supply by fluid convection and the acceleration of chemical reaction rates. Furthermore, the periodic thermal cycles of PLIH lead to a self-limited reaction process due to the limited heat diffusion within the finite irradiation pulse width in the time domain.[16]

In the proposed method, schematically depicted in **Figure 1**a, localized heating from the focused and pulsed laser irradiation onto the thin metal absorption layer induces rapid photohydrothermal synthesis only near the focal spot region, and therefore enables position-controlled deposition and bump formation of metal oxide materials within seconds. The lateral spatial resolution of this technique is limited by the laser beam spot size and thermal diffusion. For our experimental setup, the laser beam diameter at the sample surface is ≈2 μm, and the minimum dimension of a photohydrothermally grown semiconductor bump was ≈1 μm, similar to the irradiation laser wavelength (1064 nm). The details of the PLIH experimental setup are described in Figure S2, Supporting Information.

K. Kwon, J. Shim, K. Choi
Department of Electrical Engineering
Korea Advanced Institute of Science and Technology
Daejeon 305-701, Korea
Dr. J. O. Lee
Department of Electrical Engineering
California Institute of Technology
Pasadena, CA 91125, USA
Prof. K. Yu
Department of Electrical Engineering
Korea Advanced Institute of Science and Technology
Daejeon, 305-701, Korea
E-mail: ksyu@kaist.edu

DOI: 10.1002/adfm.201404215

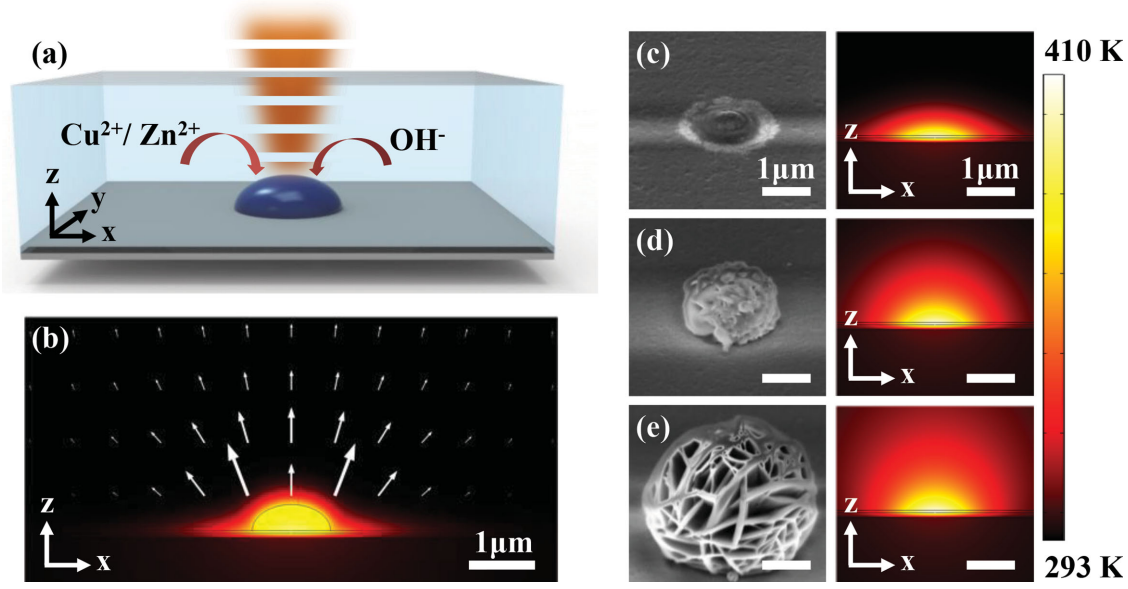

Figure 1. a) Schematic description of the focused laser heating geometry for localized hydrothermal growth of metal oxide materials on a metal absorption layer in precursor solution. The heat generated from the focused laser illumination hydrothermally converts the precursor solution into metal-oxides on the substrate. b) Temperature profile (color map) and flow velocity distribution (arrows) at 200 ns after 23.5 mW laser irradiation on a CuO bump (0.6 μm base radius and 0.4 μm height) obtained by FEM simulations. c–e) SEMs of CuO bumps grown on a 40-nm-thick tungsten film with different laser pulse widths. The corresponding temperature distribution profiles from the FEM simulations are also shown. The bumps are generated by 40-s pulsed illumination with the peak pulse power of 23.5 mW and the pulse width of 400 ns c), 4000 ns d), and 40000 ns e), respectively. The duty ratio is fixed at 10%. The FEM simulation results indicate more thermal diffusion with longer laser pulse widths. Under the short pulse width, CuO is highly confined at the substrate, but, with the longer pulse widths, CuO bumps take on the morphology of a bulk-heated case. All scale bars represent 1 μm.

Further reduction of spatial resolution can be achieved with, for example, shorter laser wavelengths and super-resolution focusing techniques beyond the diffraction limit.[17] The bump formation location can also be precisely controlled by scanning the sample stage and/or the laser beam spot. In contrast, it is usually difficult to achieve direct and real-time placement of 3D micro/nanostructures at a desired location with such precision using the conventional metal-oxides synthesis/deposition methods, such as chemical vapor deposition[18] and sputtering.[19] To obtain more insight on our rapid synthesis process, we will explain the details of the growth mechanism of the photohydrothermally synthesized metal-oxides.

2. Results and Discussion

2.1. Growth Rate

The temperature distribution as well as the heat and mass transfer of the precursor solution near the laser focal spot intimately affects the chemical reaction and thus the material growth rate in our photohydrothermal synthesis technique. PLIH allows a rapid localized growth of material compared to the conventional techniques because it can provide higher local temperature and sufficient mass transfer to facilitate the hydrothermal synthesis reaction.

First, with regard to the local temperature, the material growth rate exponentially increases with temperature since the supplementation rate of hydroxide (OH^-) is rapidly increased by the decomposition of the OH^- supplier, such as hexamethylenetetramine (HTMA) and potassium hydroxide (KOH),[20,21] due to its Arrhenius-type temperature dependence. Unlike conventional large-area hydrothermal synthesis methods in which the reaction temperature is limited by the boiling point of the precursor solution, the wavelength-scale high-intensity heating spot in PLIH can yield a spatially localized superheating condition much above the typical boiling temperature.[13] Furthermore, the repetitive thermal cycles of periodic heating and cooling also prevent undesirable bubble generation, which can adversely affect the growth process by preventing the precursor supply, introducing unpredictable growth, and/or vapor pressure-induced structure destruction. Consequently, the chemical reactions take place in a much higher temperature environment than the conventional hydrothermal synthesis techniques, resulting in ultrafast growth of metal-oxides. PLIH significantly enhances the rate of chemical reactions and material growth when compared to the continuous heating case with the same average power consumption. Figure 1b illustrates an example of temperature distribution at 200 ns after the onset of 23.5 mW laser irradiation on a hemispherical copper oxide bump (0.6 μm base radius).

Another important factor that governs the material growth rate is the reagent mass transport and local precursor concentration. PLIH induces stronger convection compared to continuous bulk heating. Given water's low thermal conductivity, thermal conduction in aqueous precursor solution is quite slow, thus, the fast heat conduction in the metal absorption layer causes a large temperature gradient and fast fluid flow in response to the transient laser illumination. As a result,

the precursor supply is significantly enhanced as depicted in Figure S3, Supporting Information. For comparison, under continuous-wave illumination with the same average intensity, fluid velocity hardly changes and remains slow (Figure S4, Supporting Information). The extreme thermal gradient leads to the efficient mass transport of precursor molecules and accelerates the hydrothermal synthesis process. The tightly focused heating spot, a feature of our system, also reduces precursor consumption and allows wavelength-scale direct patterning.

2.2. Morphology

Geometrical and morphological control of hydrothermally synthesized metal-oxides is another important issue.[22] In the suggested method, the morphology of the grown metal oxide materials can be controlled by the synthesis temperature profile and its temporal variation, similar to the way the temperature and volume/shape of solder bumps control the detailed soldering condition in conventional soldering. Material growth during hydrothermal synthesis can be divided into the nucleation and growth stages.[20] At low temperatures, the OH^- concentration is not high enough for nucleation, while crystal growth from the existing seed material can still occur. However, at higher temperatures, the increased OH^- concentration supports a higher supersaturation concentration, and, as a result, nucleation prevails, resulting in the growth of denser metal oxide materials.

Heating cycles are another important factor affecting morphology variation in the photohydrothermal synthesis of metal-oxides. With short-pulse-width PLIH (<1 μs), thermal energy is highly confined only near the metal absorption layer during the illumination, and thus its peak temperature becomes much higher than that of the grown metal-oxides and surrounding precursor solution. As a result, the metal-oxide growth occurs near the metal absorption layer rather than from the end of the existing metal-oxides structure, and therefore highly dense metal-oxides can be obtained with repeated synthesis cycles (Figure S5, Supporting Information). Furthermore, as it grows, the heat capacity increases with its volume, while at the same time the available heat flux is restricted by the incident laser power and pulse width. The reduced reaction rate thus limits the eventual dimensions of the synthesized metal oxide material.

2.3. Simulations and Experimental Results

For experimental demonstration of the PLIH-based in situ photohydrothermal synthesis method, well-known metal oxide materials such as CuO and ZnO were chosen. First, isolated CuO bumps were photohydrothermally synthesized on a thin tungsten metal absorption layer (40 nm thickness) by various laser pulse widths ranging from 400 to 40 000 ns as shown in Figure 1c–e. The pulse widths of at least 400 ns were chosen to allow enough time to reach the peak temperature during the illumination, and a fixed duty ratio of 10% was used for enough cooling time between pulses. Relatively high laser peak power (23.5 mW) was used to achieve the superheating condition in PLIH (Figure S3, Supporting Information). When the duration of laser irradiation is relatively short (e.g., 400 ns pulse width), the high temperature region is restricted to only near the metal absorption layer, resulting in shallow and dense bumps (Figure 1c). However, increased pulse widths allow enough time for heat conduction and diffusion into precursor solution. With longer pulse widths, the bump morphology becomes similar to the large-area bulk-heated case[11,23] (Figure 1e). Therefore, a shorter laser pulse width (400 ns pulse width and 4000 ns period) was selected to produce dense and packed semiconductor bumps in the following experiments.

To experimentally verify the effects of the photohydrothermal synthesis temperature, CuO and ZnO bumps were synthesized by various laser powers as shown in **Figure 2**a for CuO as well as Figures 2b and S6, Supporting Information for ZnO. CuO (ZnO) synthesis was observed beyond the laser peak power of 23.5 mW (15.4 mW) because the typical synthesis temperature of CuO is known to be higher than ZnO.[11,23] In both cases, lump-like hemispherical bumps were observed, rather than the nanowires or nanorods morphologies which are typical products of conventional large-area hydrothermal synthesis. These unique configurations result from the limited thermal diffusion of PLIH as explained before. The nucleation-dominant crystal growth occurs at elevated reaction temperatures much above the typical water boiling point only near the laser beam spot. For both CuO and ZnO, ultrafast growth rates and micrometer-scale growth in a few seconds were observed, whereas conventional techniques with bulk-heating typically yield micrometer-long growth in hours.[11,23] The base diameters of the isolated bumps were self-limited and bounded by the laser spot size of ≈2 μm even at high peak powers.

To further explore temperature dependence, the detailed effects of temperature and illumination time on the material growth rate are demonstrated in Figure 2c,d for ZnO synthesis. The ZnO bump volumes as a function of laser irradiation time and peak power are represented in Figure 2c, indicating the saturation of the growth rate with the increase of synthesis time. Figure 2d shows the relationship between the ZnO bump volume and the estimated synthesis temperature. According to the Arrhenius equation, the synthesized metal oxide material volume is proportional to the chemical reaction rate constant proportional to $\exp(E_a/RT)$, where E_a is the activation energy, R is the gas constant, and T is temperature in Kelvin. In the logarithmic scale, the synthesized material volume is inversely proportional to the temperature and the extracted slopes in Figure 2d are all similar to each other and roughly proportional to E_a/R. When the bump volume becomes large enough, however, the slope does not follow this trend due to the growth rate saturation.

To investigate such self-limited growth effects, computer simulations based on the finite element methods (FEM) were performed according to the bump dimensions and the laser irradiation powers. **Figure 3**a,b shows the temperature distributions with the peak laser irradiation powers of 23.5 and 55.9 mW, respectively. The ZnO bump dimensions in the simulations were estimated from the inset scanning electron micrograph (SEM) images and its thermal conductivity was assumed to be 60 $W\ m^{-1}\ K^{-1}$.[24] The temperature profiles along the z-axis at the center for each case are also plotted in Figure 3c,d, which indicate that the temperature of the ZnO material is much higher than the typical hydrothermal synthesis temperature at the initial stage (0.2 s). After

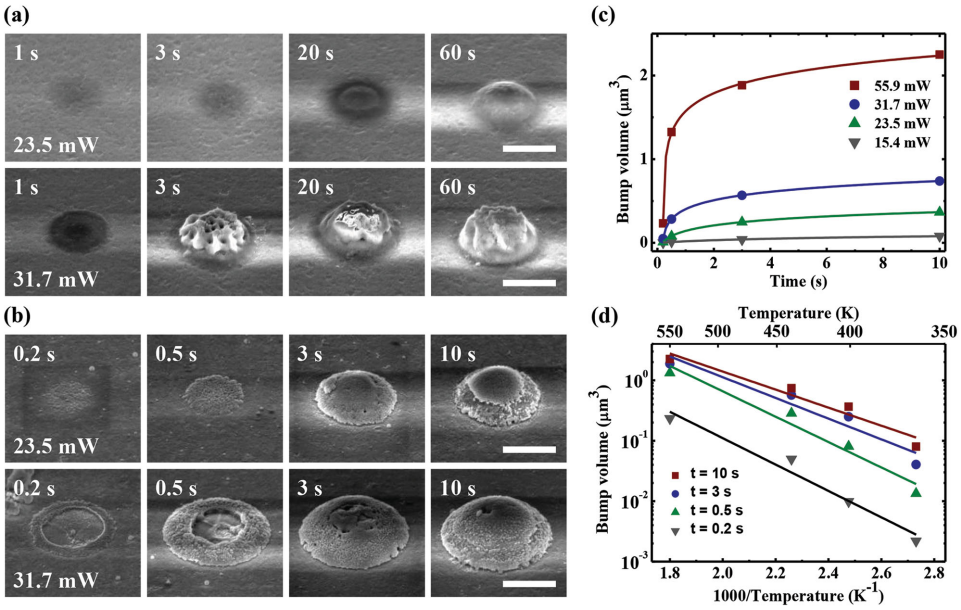

Figure 2. Growth and morphological characteristics of the laser-based photohydrothermal synthesis process on the planar metal absorption layer. a) SEMs of CuO bumps on the 40-nm-thick tungsten film for various laser peak powers (23.5 and 31.7 mW) and growth times (from 1 to 60 s). Generation of vapor at 31.7 mW peak power causes uneven bump structures with voids, while packed CuO synthesis was observed at 23.5 mW. b) SEMs of ZnO bumps on the same tungsten film for various laser peak powers (23.5 and 31.7 mW) and growth times (from 0.2 to 10 s). At high laser intensities (31.7 mW case), the vapor layer develops at the early stage of the synthesis process. c) ZnO bump volume as a function of the growth time. As the bump volume increases, the growth rate is saturated due to the increased heat capacity. d) Relationship between the synthesized ZnO volume and the peak temperature shows Arrhenius dependence. All scale bars represent 1 μm.

it has grown up, however, the increased heat capacitance limits the peak temperature and the heat flux barely reaches the liquid–solid interface due to the short pulse width. As a result, the peak temperature at the liquid–solid interface after 3 s becomes much lower and the deceleration of the synthesis rate results self-limited growth.

The interesting morphological features of the metal-oxides observed in Figure 2a,b are from their different construction mechanisms depending on the illumination power. In CuO synthesis, CuO was synthesized as a packed hemispherical bump when the metal absorption layer was heated by 23.5 mW peak power, but uneven bump structures with small voids were

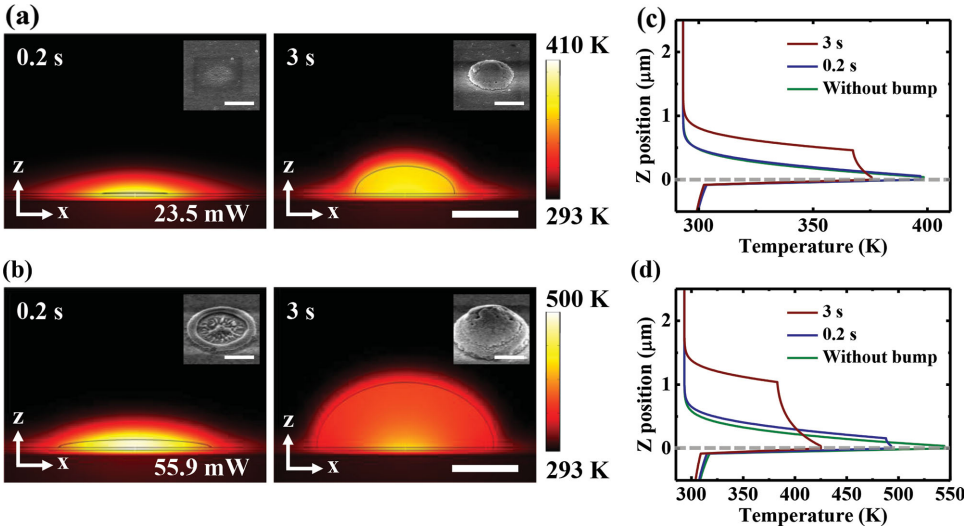

Figure 3. Illumination power and temperature dependence of metal-oxides bump size. a,c) and b,d) are the simulated temperature profiles with the incident laser peak powers of 23.5 and 55.9 mW, respectively. The ZnO bump dimensions were estimated from the inset SEMs from Figure S6, Supporting Information. a) and b) represent the temperature distributions at 0.2 and 3 s, while c) and d) show the detailed temperature profile along the *z*-axis at the center for the laser irradiation powers of 23.5 and 55.9 mW, respectively. The gray dashed lines at $z = 0$ indicate the location of the metal absorption layer. The increased heat capacity from the growth of the metal-oxides limits the peak temperature and the heat flux barely reaches the edge of the metal-oxide due to the short laser pulse width. All scale bars represent 1 μm.

obtained with higher peak power heating (e.g., 31.7 mW in Figure 2). For ZnO, packed hemispherical solder bumps eventually grew up after a long growth time (10 s) regardless of the laser input power, but for short growth time (less than 1 s) its morphology was quite different. Under low power irradiation, a film-like morphology was obtained, but at higher irradiation powers crater-like shapes were observed.

To verify the reason for such morphological differences produced by varying the input laser peak power, a temporal temperature distribution profile according to the laser power in PLIH was examined by computer simulations (Figure S3, Supporting Information). As the laser irradiation peak power increased, the maximum local temperature near the laser beam spot reached its maximum, and then quickly came back to room temperature during the cooling cycle after the laser illumination is turned off. When the sample was illuminated with a laser peak power of 23.5 mW, void-free metal oxide bumps could be obtained beyond the boiling point of water. Such superheating phenomenon usually occurs when the heating spot is too small to overcome hydraulic pressure and surface tension. At even higher laser irradiation powers, on the other hand, the local temperature rises over the superheating temperature limit (or spinodal point) and vapor nucleation takes place.[13] Vapor seeds begin to expand into the larger vapor layer when its pressure exceeds the surrounding fluidal pressure. The presence of the vapor layer at the center of the laser beam spot screens the precursor supply preventing the metal oxide growth (Figure S1b, Supporting Information). The hydrothermal synthesis reaction, however, can still occur outside the vapor edge where temperature is high enough for hydrothermal processes, and finally results in the crater-like ring morphology shown in the early stages of high-intensity laser irradiation for ZnO growth (31.7 and 55.9 mW cases in Figure S6, Supporting Information). As the ZnO ring grows up from the perimeter of the vapor layer, the heat capacity increases and the absorption layer temperature decreases, which in turn reduces vapor layer formation. Hence, bump-like ZnO can be eventually formed after long growth time (>3 s) even when the initial local temperature is higher than the spinodal point. For further investigation of material properties, Raman and photoluminescence measurements as well as energy-dispersive X-ray spectroscopy were performed for photohydrothermally grown CuO and ZnO materials as described in Figures S7–S10, Supporting Information.

2.4. Applications

Joining micro/nanoscale components, such as nanowires, is important to form functional devices and various approaches have been developed including welding[25] and soldering.[26] They, however, mostly relies on complicated processes and requires vacuum conditions, which hinder a facile in situ operation. We demonstrate that our proposed method can be used to interconnect separated submicrometer-scale metal structures with a submicrometer gap and allow semiconducting functions. Because of the semiconducting properties of metal oxide materials, the proposed real-time in situ photohydrothermal synthesis provides interesting electrical/optoelectronic functionalities in addition to the conventional joining/soldering processes whose use is mainly restricted to electric conduction and mechanical assembly.

Figure 4 shows in situ electrical/mechanical interconnection of two separated tungsten metal strips with ZnO

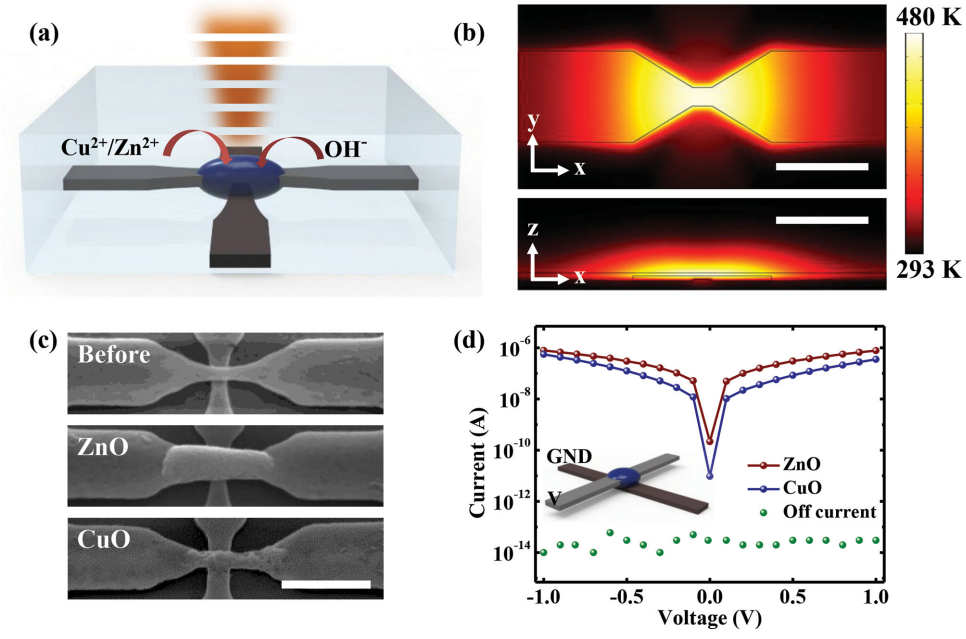

Figure 4. Electrical connection and soldering by laser-based localized photohydrothermal synthesis of metal-oxides. a) Schematic diagram of microsoldering via synthesized metal-oxides in aqueous precursor solution. b) Simulated temperature profile (top and side view) at 200 ns after 23.5 mW laser irradiation incident on a suspended tungsten metal strip. Thermal energy is highly confined around the center of the metal bridge. c) SEMs of the crossed metal strips before and after photohydrothermal metal-oxides (ZnO and CuO) synthesis. d) Current–voltage characteristics between the metal strips before and after the metal-oxides synthesis. Scale bars represent 1 μm.

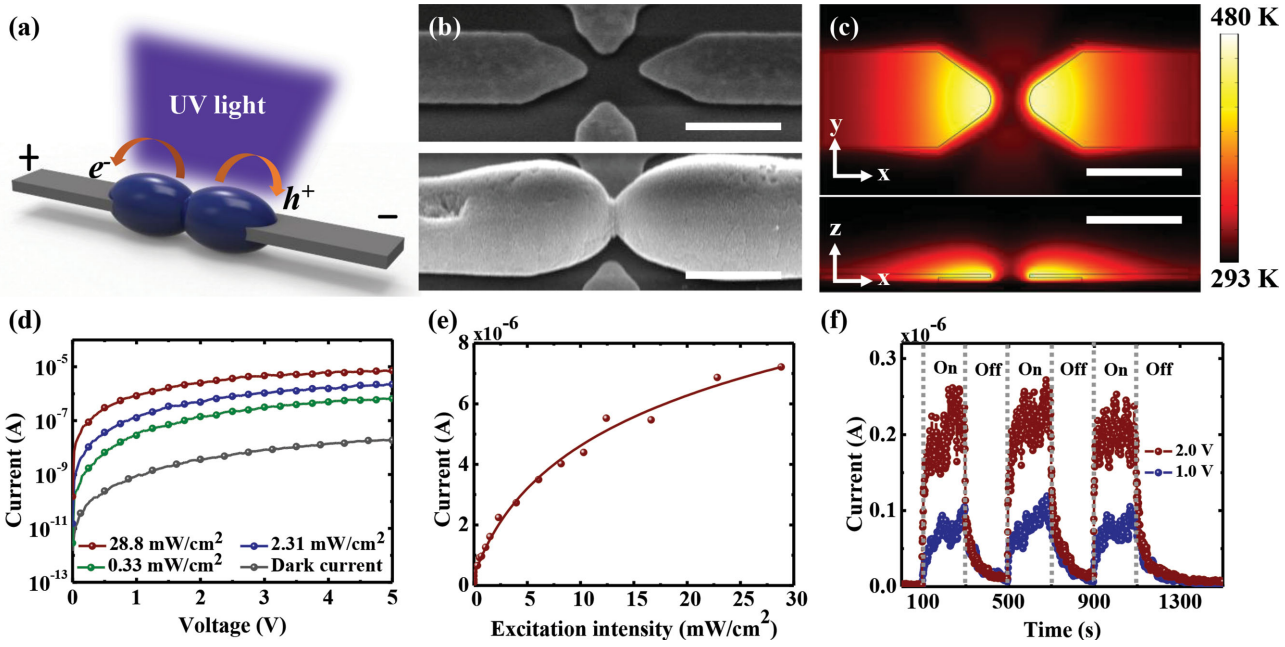

Figure 5. UV detection from the photohydrothermally synthesized metal-oxides bump. a) Schematic diagram of a UV detection scenario with a ZnO solder bump connecting two metal electrodes. b) SEM of the tungsten electrodes connected by the synthesized ZnO material. A 500 nm gap between tungsten electrodes was fabricated and separately grown ZnO bumps connect two separate metal strips after the photohydrothermal process. c) Simulated temperature profile (top and side view) at 200 ns after 23.5 mW laser irradiation. d) Current–voltage characteristics between the metal strips with different UV light intensities. e) Measured photocurrent as a function of the incident UV intensity with a 5 V applied bias. f) Time-resolved photocurrent generation with 1 and 2 V external biases. Scale bars represent 1 μm.

and CuO, similar to the conventional soldering process. For experimental demonstration, we fabricated a 40-nm-thick tungsten metal bridge structure suspended over the bottom metal strip (crossed metal strips as shown in Figure 4c). The vertical gap distance between the top and bottom metal line is 50 nm. The metal strips are connected in a few seconds with metal oxide semiconductor materials by the proposed selective photohydrothermal process using PLIH. It is worth noting that multiple semiconducting metal oxide materials can be additively synthesized/deposited at desired locations by exchanging precursor solutions and repeating the localized photohydrothermal synthesis process multiple times. It is also possible to connect a wider gap distance (500 nm lateral gap) as shown in **Figure 5**.

Figure 4b shows the temperature profile at 200 ns after the onset of 23.5 mW laser irradiation on the suspended metal strip. The tightly focused beam spot and rapid thermal cycles in PLIH allow that thermal energy is highly restricted near the center of the suspended metal strip for soldering of two separated metal strips. For electrical characterization, precursor solution is removed after the soldering process. Figure 4d shows that the metal strips are indeed electrically connected; the resistances of the ZnO and CuO solder joins are estimated to be 1.26 and 1.79 MΩ, respectively. According to our FEM-based electrical simulation (Figure S11, Supporting Information), they correspond to 0.583 and 0.405 S m^{-1}, respectively, which are within the typical conductivity range of ZnO[27] and CuO.[28] The exact solder resistance is influenced by many factors, including the bump size, annealing temperature/time, and contact resistance. For example, additional thermal annealing processes improve the solder resistance as described in Figure S12, Supporting Information.

The proposed photohydrothermal soldering of metal oxide materials between metal electrodes can also provide a simple and effective means of UV light detection through photo-induced electron–hole pair generation (Figure 5). To demonstrate in situ metal-oxides formation capable of UV detection, we joined the disconnected tungsten metal strips with the lateral gap of 500 nm using the photohydrothermal synthesis of ZnO bumps. The size of the synthesized ZnO materials on the both sides of the metal strips grew with the laser heating time and they finally formed a connected bridge structure as shown in Figure 5b. The overall shape of the bridge structure resembles the temperature distribution simulation results shown in Figure 5c. Figure 5d–f shows the electrical measurement results for the UV detecting metal-oxides connections between two metal electrodes. Typical current–voltage characteristics with and without UV illumination (365 nm center wavelength) indicate a significant increase in current flow under UV illumination (Figure 5d). By varying the UV intensity from 0.33 to 28.8 mW cm^{-2}, the measured photocurrents were increased from one to three orders of magnitude as compared to the dark current level. It is well-known that the photogenerated holes in single-crystalline ZnO nanowires travel to the surface and are trapped at the oxygen-related hole trapping states, which provide a long electron life time due to the unbalance between electrons and holes, resulting in high photoconductivity.[7] Large photocurrent enhancements in our measurements also result from the dangling-bonds-induced trap states at the grown zinc oxide surface.

Due to the Schottky barriers at the metal–semiconductor (W–ZnO) junction, the current versus voltage curves show exponential growth at low applied biases. However, the photocurrent starts to increase linearly with higher applied biases due to the enhancement of the carrier drift velocity. The dependence of the photocurrents on the UV illumination intensities at an applied bias of 5 V is shown in Figure 5e. At low UV intensity levels, the photocurrent increases linearly with the illumination intensity, indicating that the number of photo-generated carriers is proportional to the absorbed optical power. However, it starts to saturate under the higher illumination intensities. This sublinear dependence results from the reduction of hole-trapping states and photocarrier lifetimes, similar to the single-crystalline ZnO nanowire case.[7] Under the high-intensity UV illumination, the hole traps are filled with photo-generated holes and the number of free holes increases, hence the probability of electron–hole recombination significantly increases.

Figure 5f shows the dynamic photoresponses at room temperature with two different external biases. UV illumination is switched on and off periodically at intervals of 200 s. Upon UV illumination (4 mW cm^{-2}), the currents through the ZnO connection increase from ≈500 pA (≈2 nA) to ≈100 nA (≈250 nA) at a 1 V (2 V) bias voltage.

3. Conclusion

In summary, we have demonstrated a laser-based photothermal route for real-time in situ soldering and selective deposition of metal oxide semiconductor materials on metal surfaces in precursor solution environments. The proposed technique takes advantage of the thermodynamics of localized PLIH, providing accelerated speed and accurate control of the hydrothermal material growth process at elevated temperatures much above the boiling point. The process is naturally self-limited owing to the strong dependence of the temperature and the bump volume of the synthesized metal-oxides. High-intensity focused laser pulses provide ultrafast and precise material synthesis via high local temperature and rapid mass transfer. The proposed laser-based photohydrothermal synthesis method allows a simple and facile growth process with restricted material volumes and can provide new levels of control for placing metal oxide materials at desired locations and thereby joining micro/nanoscale metallic building blocks such as metal nanowire-based meshes and circuits. Furthermore, taking advantages of semiconducting properties of metal oxide materials, the proposed technique may open up numerous applications in heterogeneous electric and optoelectronic interconnections with resistive, memristive, gating, and/or rectifying device components.

4. Experimental Section

PLIH Experimental Setup: A schematic diagram of the experimental setup for the localized photohydrothermal synthesis of metal oxide materials with focused laser beam irradiation is illustrated in Figure S2, Supporting Information. A droplet of precursor solution (≈100 μm height) for hydrothermal metal oxide synthesis is first placed on the sample surface and then covered with a cover glass to prevent possible evaporation. The details of the sample fabrication method and precursor solution can be found in the following sections. For localized laser heating, the collimated output light from a 1064-nm pulsed semiconductor laser diode was focused by a 100x objective with a numerical aperture of 0.5. The laser beam diameter at the sample surface is ≈2 μm. Tungsten material was selected as the light absorption layer in our experiments for reasonable absorption at 1064 nm. Other metal layers such as gold and aluminum can also be used with shorter visible wavelength lasers for maximum absorption. The objective lens, together with an image sensor and a visible illumination unit, was also used for real-time imaging of the sample surface and the reflected laser light.

Sample Preparation: Tungsten Absorption Layer – A 10-nm-thick thermal oxide layer was first grown on a silicon substrate and then a 20-nm-thick silicon nitride layer and an additional 50-nm-thick silicon dioxide layer were deposited using chemical vapor deposition techniques for thermal insulation. A final 40-nm tungsten material was sputtered to form the metal absorption layer. Metal Bridge Structure – We used tungsten metal bridges suspended over the bottom metal layer prepared by the above method with additional patterning steps. The thicknesses of the upper and lower tungsten metal layers were 40 and 20 nm, respectively, and the air gap between them was ≈50-nm-thick. The details of the fabrication process can be found in ref. [29].

Precursor Solution Preparation: ZnO Precursor – An aqueous solution mixture of 25×10^{-3} M zinc nitrate ($Zn(NO_3)_2$, Sigma-Aldrich) and 25×10^{-3} M HTMA ($(CH_2)_6N_4$, Sigma-Aldrich). CuO Precursor – An aqueous solution mixture of 50×10^{-3} M copper nitrate trihydrate ($Cu(NO_3)_2{\cdot}3H_2O$, Sigma-Aldrich) and 25×10^{-3} M HTMA ($(CH_2)_6N_4$, Sigma-Aldrich).

Simulation Method: To analyze the metal-oxides bump formation on the metal absorption layer, numerical computer simulations based on the finite-difference time-domain (FDTD) technique and FEM were conducted (FDTD Solutions, Lumerical Solutions Inc., and COMSOL Multiphysics, COMSOL, Inc.). The reflected laser power from the sample surface was first calculated by the FDTD simulations and found to be ≈60% of the input light for the 40 nm-thick tungsten film. The optical beam intensity profile was assumed to follow the Gaussian function with a radius of ≈1 μm. Heat transfer, thermal distribution, and fluid transport by both conduction and convection with volumetric force were then subsequently calculated from the absorbed power profile. The thermal conductivity of ZnO and CuO material were estimated to be 60 and 17 W m^{-1} K^{-1}, respectively.[30] For the 3D temperature profile of the metal bridge structure shown in Figures 4 and 5, 3D simulation model with radio frequency and heat transfer modules was used. The thermal conductivity of the tungsten strips was assumed to be 174 W m^{-1} K^{-1}.

Electrical Characterization: A probe station with a semiconductor analyzer (HP4156A, Hewlett-Packard) in a dark Faraday cage was used to measure the current–voltage characteristics. For UV detection measurements, the metal bridge with the zinc oxide connection was placed in the probe station, and illuminated by UV light (365 nm center wavelength) from a high-power light emitting diode (M365L2, Thorlabs, Inc.).

Supporting Information

Supporting Information is available from the Wiley Online Library or from the author.

Acknowledgements

This work was supported by the Center for Integrated Smart Sensors and the Center for Advanced Meta-Materials funded by the Ministry of Science, ICT and Future Planning as Global Frontier Project (CISS-2012M3A6A6054191 and CAMM-2014M3A6B3063709) and the National Research Foundation of Korea (NRF) grant funded by the Korean

Government (Ministry of Education and Science Technology) (2008-0062256). The authors would like to thank Prof. Jun-Bo Yoon at KAIST for his support in device fabrication.

Received: November 27, 2014
Revised: January 12, 2015
Published online: February 12, 2015

[1] P. Cox, *Transition Metal Oxides*, Clarendon Press, Oxford, UK **1992**.
[2] A. Janotti, C. G. Van de Walle, *Rep. Prog. Phys.* **2009**, *72*, 126501.
[3] Z. Zhang, P. Wang, *J. Mater. Chem.* **2012**, *22*, 2456.
[4] a) J. Song, Y. Zhang, C. Xu, W. Wu, Z. L. Wang, *Nano Lett.* **2011**, *11*, 2829; b) A. Sawa, *Mater. Today* **2008**, *11*, 28.
[5] M. S. Arnold, P. Avouris, Z. W. Pan, Z. L. Wang, *J. Phys. Chem. B* **2003**, *107*, 659.
[6] B. Ryu, Y. T. Lee, K. H. Lee, R. Ha, J. H. Park, H.-J. Choi, S. Im, *Nano Lett.* **2011**, *11*, 4246.
[7] C. Soci, A. Zhang, B. Xiang, S. A. Dayeh, D. Aplin, J. Park, X. Bao, Y.-H. Lo, D. Wang, *Nano Lett.* **2007**, *7*, 1003.
[8] C. Pan, L. Dong, G. Zhu, S. Niu, R. Yu, Q. Yang, Y. Liu, Z. L. Wang, *Nat. Photonics* **2013**, *7*, 752.
[9] A. Kolmakov, M. Moskovits, *Annu. Rev. Mater. Res.* **2004**, *34*, 151.
[10] Y. Zhang, K. Yu, D. Jiang, Z. Zhu, H. Geng, L. Luo, *Appl. Surf. Sci.* **2005**, *242*, 212.
[11] L. E. Greene, M. Law, J. Goldberger, F. Kim, J. C. Johnson, Y. Zhang, R. J. Saykally, P. Yang, *Angew. Chem. Int. Ed.* **2003**, *42*, 3031.
[12] M. Cao, C. Hu, Y. Wang, Y. Guo, C. Guo, E. Wang, *Chem. Commun.* **2003**, 1884.
[13] M. T. Carlson, A. J. Green, H. H. Richardson, *Nano Lett.* **2012**, *12*, 1534.
a) J. Yeo, S. Hong, M. Wanit, H. W. Kang, D. Lee, C. P. Grigoropoulos, H. J. Sung, S. H. Ko, *Adv. Funct. Mater.* **2013**, *23*, 3316; b) J. Shim, K. Kwon, K. Yu, presented at *2012 International Conference on Optical MEMS and Nanophotonics (OMN)* , Banff, AB, Canada August **2012**.
[14] E. Lukianova-Hleb, Y. Hu, L. Latterini, L. Tarpani, S. Lee, R. A. Drezek, J. H. Hafner, D. O. Lapotko, *ACS Nano* **2010**, *4*, 2109.
[15] G. Baffou, R. Quidant, *Chem. Soc. Rev.* **2014**, *43*, 3898.
[16] E. T. Rogers, J. Lindberg, T. Roy, S. Savo, J. E. Chad, M. R. Dennis, N. I. Zheludev, *Nat. Mater.* **2012**, *11*, 432.
[17] C. Rao, S. Vivekchand, K. Biswas, A. Govindaraj, *Dalton Trans.* **2007**, *34* , 3728.
[18] P. Samarasekara, N. Kumara, N. Yapa, *J. Phys.: Condens. Matter* **2006**, *18*, 2417.
[19] Z. Zhou, Y. Deng, *J. Phys. Chem. C* **2009**, *113*, 19853.
[20] H. Hayashi, Y. Hakuta, *Materials* **2010**, *3*, 3794.
[21] J. Joo, B. Y. Chow, M. Prakash, E. S. Boyden, J. M. Jacobson, *Nat. Mater.* **2011**, *10*, 596.
[22] M. Vaseem, A. Umar, S. H. Kim, Y.-B. Hahn, *J. Phys. Chem. C* **2008**, *112*, 5729.
[23] S. Kasap, P. Capper, *Springer Handbook of Electronic and Photonic Materials*, Springer, New Delhi, India **2007**.
[24] a) E. C. Garnett, W. Cai, J. J. Cha, F. Mahmood, S. T. Connor, M. G. Christoforo, Y. Cui, M. D. McGehee, M. L. Brongersma, *Nat. Mater.* **2012**, *11*, 241; b) Y. Lu, J. Y. Huang, C. Wang, S. Sun, J. Lou, *Nat. Nanotechnol.* **2010**, *5*, 218.
[25] a) J.-W. Do, D. Estrada, X. Xie, N. N. Chang, J. Mallek, G. S. Girolami, J. A. Rogers, E. Pop, J. W. Lyding, *Nano Lett.* **2013**, *13*, 5844; b) Y. Peng, T. Cullis, B. Inkson, *Nano Lett.* **2008**, *9*, 91.
[26] W. Lin, D. Chen, J. Zhang, Z. Lin, J. Huang, W. Li, Y. Wang, F. Huang, *Cryst. Growth Des.* **2009**, *9*, 4378.
[27] A. Parretta, M. Jayaraj, A. Di Nocera, S. Loreti, L. Quercia, A. Agati, *Phys. Status Solidi A* **1996**, *155*, 399.
[28] J. O. Lee, Y.-H. Song, M.-W. Kim, M.-H. Kang, J.-S. Oh, H.-H. Yang, J.-B. Yoon, *Nat. Nanotechnol.* **2013**, *8*, 36.
[29] a) J. Wang, M. Isshiki, in *Springer Handbook of Electronic and Photonic Materials*, Springer, New Delhi, India **2007**, 325; b) A. Edwards, *Compilation of Thermal Property Data for Computer Heat-Conduction Calculation* California Univ., Livermore, Livermore, CA, USA **1969**.